Superplastic behavior of friction-stir welded Al−Mg−Sc−Zr alloy in ultrafine-grained condition

I. VYSOTSKIY, K. KIM, S. MALOPHEYEV, S. MIRONOV, R. KAIBYSHEV

Belgorod National Research University, Pobeda 85, Belgorod 308015, Russia

Abstract: The present work was undertaken to improve superplastic ductility of friction-stir welded joints of ultrafine-grained (UFG) Al−Mg−Sc−Zr alloy. In order to suppress the undesirable abnormal grain growth, which typically occurs in the heavily deformed base material, the UFG material was produced at elevated temperature. It was suggested that the new processing route could reduce dislocation density in the UFG structure and thus enhance its thermal stability. It was found, however, that the new approach resulted in a relatively high fraction of low-angle boundaries which, in turn, retarded grain-boundary sliding during subsequent superplastic tests. Therefore, despite the successful inhibition of the abnormal grain growth in the base-material zone, the superplastic deformation was still preferentially concentrated in the fully-recrystallized stir zone of the material. As a result, the maximal elongation-to-failure did not exceed 700%.
Key words: aluminum alloys; equal-channel angular pressing; friction-stir welding; ultrafine-grained materials; superplasticity

1 Introduction

Due to the promising combination of service properties including high strength, excellent formability, good weldability, and corrosion resistance, Al−Mg−Sc alloys are widely used in industry [1]. As these alloys experience no age hardening, their strengthening is achieved either by cold working or via grain refinement [1−4]. The later process additionally benefits from superior superplastic properties [2,5,6], thus being particularly attractive. Among various grain-refinement techniques, equal-channel angular pressing (ECAP) is often considered the most effective approach for the production of bulk ultrafine-grained (UFG) materials [5−7]. In practice, ECAP is sometimes combined with subsequent rolling to obtain the UFG sheets. However, the limited dimensions of such sheets essentially limit their application for the fabrication of large-scale structures via superplastic forming. One of the simplest ways to overcome this problem is the joining of several UFG sheets into a single package. As conventional fusion welding cannot preserve the UFG structure, an innovative friction-stir welding (FSW) technique is often considered the most promising method for this purpose. This solid-state approach involves very large plastic strains which normally produce fine-grained structure in the weld zone [5,8−12].

In the previous works, it has been found that the superplastic behavior of such joints is not uniform [10,13]. Specifically, the UFG structure in the base-material zone experienced an abnormal grain growth, which essentially degraded superplastic ductility. Accordingly, the superplastic deformation was localized primarily in the stir zone.

This undesirable effect has been attributed to the relatively high dislocation density in the heavily deformed base material [13].

To the best of the authors' knowledge, no recent work has been reported in this area and therefore the above problem still remains unsolved. Therefore, the present study aimed at overcoming it. To this end, the prior severe plastic deformation step was conducted at elevated temperature. This approach was suggested to reduce dislocation density in the fine-grained material, thereby suppressing the undesirable abnormal grain growth during subsequent superplastic forming. In turn, this should provide a nearly uniform distribution of superplastic strain in a friction-stir welded joint and thus eventually enhance its global ductility.

2 Experimental

The material used in the present study was a commercial 1570C alloy (As per Russian classification) with the nominal chemical composition of Al−5.4Mg−0.37Mn−0.2Sc−0.09Zr−0.29Ti−0.07Fe−0.04Si (all in wt.%). It was produced by semi-continuous casting and then undergone an annealing treatment at 360 °C for 8 h to provide the uniform precipitation of coherent nano-scale $\beta'(Al_3(Sc,Zr))$-dispersoids. To produce the UFG structure, the heat-treated material was extruded to 75% of cross-sectional area reduction (from $d400$ mm to $d\approx200$ mm) at 380 °C. Then, the billets measuring 180 mm × 180 mm × 40 mm were machined from the extruded material and subjected to ECAP via B_C route to the true accumulated strain of ~12.0 at 300 °C. From the ECAPed billets, the sheets measuring 100 mm × 100 mm × 10 mm were cut and then rolled at 300 °C to the final thickness of 2 mm (i.e., 80% of rolling reduction). The obtained material condition was referred to as base material throughout the manuscript.

From the hot-rolled base material, the plates measuring 100 mm × 100 mm × 10 mm were machined and then friction-stir butt welded using a commercial AccuStir 1004 FSW machine. FSW was performed at the tool rotation rate of 500 r/min, the tool travel speed of 150 mm/min, and the tool tilting angle of 2.5°. The welding tool was manufactured from a tool steel and consisted of a shoulder of 12.5 mm in diameter and a threaded cylindrical probe of 1.5 mm in length. To ensure the

full-penetration joining, the double-side FSW was conducted. The welding conditions were selected based on the previous experience as providing the most homogeneous microstructure distribution within the welded sheets. The conventional definition of FSW geometry was adopted, viz. welding direction (WD), transverse direction (TD), and normal direction (ND).

To examine superplastic behavior of the produced joints, tensile specimens were machined transversely to the WD, as shown in Fig. 1. Those included all microstructural zones generated during FSW, i.e., the base material zone, the stir zone, and the transition zone between them. The specimens were mechanically polished to remove the surface defects and provide a uniform thickness. The superplastic tests were conducted using an Instron 5882 universal testing machine equipped with a high-temperature chamber. The tests were performed in the range of temperatures from 350 to 450 °C and that of the nominal strain rates of 2.8×10^{-4} to $5.6\times10^{-1}\,s^{-1}$. It is important to note that all specimens were held at the test temperature for about 10 min prior to the superplastic test to achieve the thermal equilibrium. The values of strain sensitivity ($m=\mathrm{dln}\,\sigma/\mathrm{dln}\,\dot{\varepsilon}$, where σ is flow stress, and $\dot{\varepsilon}$ is strain rate) were determined by the strain-rate-jump tests [14].
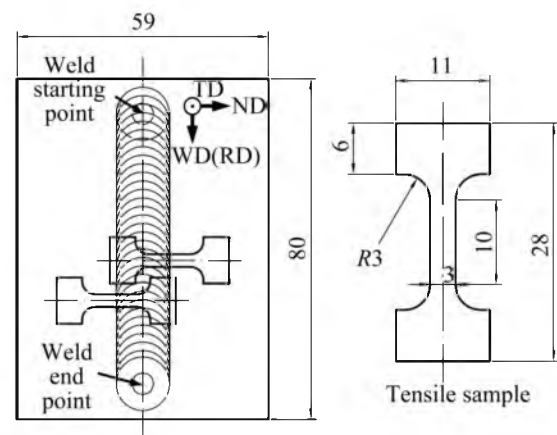

Fig. 1 Schematic showing dimensions and placement of tensile specimens relative to friction-stir joint (unit: mm)

Structural characterization was performed by the electron backscatter diffraction (EBSD) technique. The suitable surface was obtained by mechanical polishing followed by electro-polishing using a 25 vol.% nitric-acid solution in ethanol at −32 °C and a voltage of 19.5 V. EBSD was

conducted using FEI Quanta 600 field-emission-gun scanning electron microscope (FEG-SEM) equipped with TSL OIM™ software. In EBSD maps shown throughout the manuscript, low-angle boundaries (LABs) ($2°<\theta<15°$) and high-angle boundaries ($\theta \geq 15°$) were depicted as red and black lines, respectively. The linear intercept method was used for grain-size measurements [15].

3 Results

3.1 Microstructure distribution in as-welded condition

The detailed characterization of the microstructures produced in friction-stir welded material has been provided elsewhere [5,6,10]. Nevertheless, for the sake of clarity, a brief description is given in the present section.

To evaluate the broad aspects of microstructure distribution within the welded material, the microhardness profile was measured across the joint mid-thickness (Fig. 2). Although the profile encompassed three different microstructural zones (i.e., base material, transition zone, and stir zone, as indicated in the insert at the top right corner),
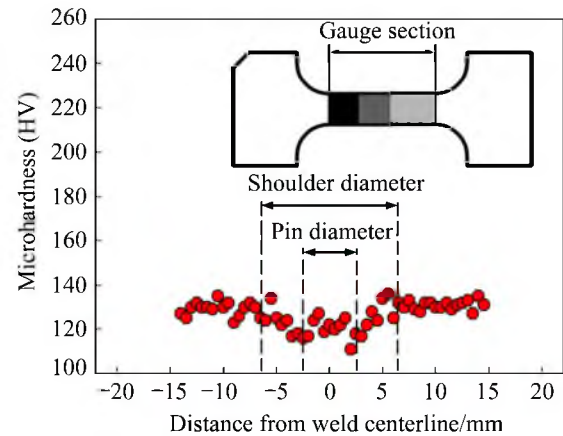

Fig. 2 Microhardness profile measured across weld mid-thickness (In the tensile specimen shown at the top right corner, black, grey, and light-grey areas depict stir zone, transition zone, and base material, respectively)

only subtle material softening was revealed in the transition and stir zones. Therefore, the microhardness measurements suggested comparatively small microstructural variations.

To provide a closer inspection of the microstructures produced during FSW, EBSD maps were taken from different zones and shown in Fig. 3.
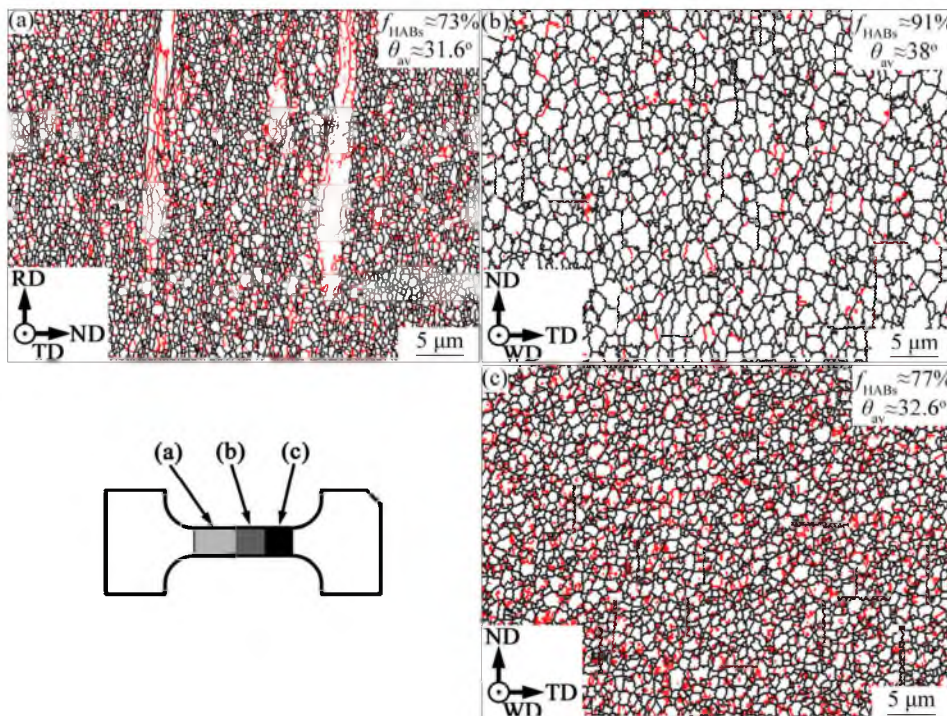

Fig. 3 EBSD grain-boundary maps taken from base material (a), transition zone (b), and stir zone (c) (In the maps, LABs and HABs are depicted as red and black lines, respectively. f_{HABs} and θ_{av} in the inserts at the top right corners of the figures indicate HAB fraction and the average misorientation, respectively. RD, WD, ND, and TD denote rolling direction, welding direction, normal direction, and transverse direction, respectively)

In the base material zone, the microstructure was bimodal (Fig. 3(a)). It was dominated by nearly equiaxed ultra-fine grains (~0.7 μm in size), but also contained a notable portion of coarse-grained remnants. Another important issue was a relatively high LABs fraction. These microstructural aspects are thought to be associated with the continuous dynamic recrystallization (cDRX) which presumably operated during ECAP and/or hot rolling of the studied material [5,6,10]. On the other hand, dislocation density was found to be as low as ~9×10^{13} m^{-2} [5,6], presumably due to the relatively high processing temperature (i.e., 300 °C). It is also worth noting that the base material contained coherent Al_3(Sc,Zr) dispersoids with an average size of ~9 nm which were uniformly distributed in grain interiors [5,6].

The microstructure of the transition zone (Fig. 3(b)) was dominated by the almost fully-recrystallized grains of ~1.5 μm in diameter. The fraction of HABs was as high as ~90%. It should be noted that the transition region in the friction-stir welded material was composed mainly of the heat-affected zone (HAZ), in which the welded material experienced only thermal exposure during FSW. Hence, the microstructure revealed in Fig. 3(b) presumably originated from the static recrystallization and grain growth of the base material.

In the stir zone, the microstructure consisted of the fully-recrystallized ~1 μm grains (Fig. 3(c)), which were typically associated with cDRX operating during FSW [7,16]. Accordingly, HABs fraction was relatively high (~77%) whereas

dislocation density was as low as ~5×10^{13} m^{-2} [5,10]. It is also important to notice that the coherent Al_3(Sc,Zr) dispersoids almost completely preserved during FSW, and the mean particle size of 9 nm remained virtually unchanged [10].

Therefore, although the careful control of FSW conditions was undertaken in the present study, the microstructure distribution in the welded material was not entirely uniform. This effect was presumably associated with very large gradients of temperature, strain, and strain rate inherent to the FSW process.

3.2 Mechanical behavior during superplastic tests

The characteristic deformation diagrams recorded during superplastic tests of the welded joints at different temperatures are shown in Fig. 4(a). The relevant superplastic characteristics were summarized in Table 1 and Figs. 4 and 5. In the entire studied range, the total elongation-to-failure exceeded 200% (Table 1), i.e., the welded material exhibited superplastic properties [17,18]. The deformation curves were broadly similar to that usually observed during superplastic tests of UFG Al−Mg−Sc alloys obtained by ECAP [17], FSP [11,19] or FSW [10]. In all cases, the deformation diagrams were characterized by an immediate hardening upon yielding, the following smooth peak, and the final pronounced softening stage. No obvious steady-state flow was observed. As expected, the increase in deformation temperature resulted in smoothing of the strain hardening effect but promoted the softening stage.
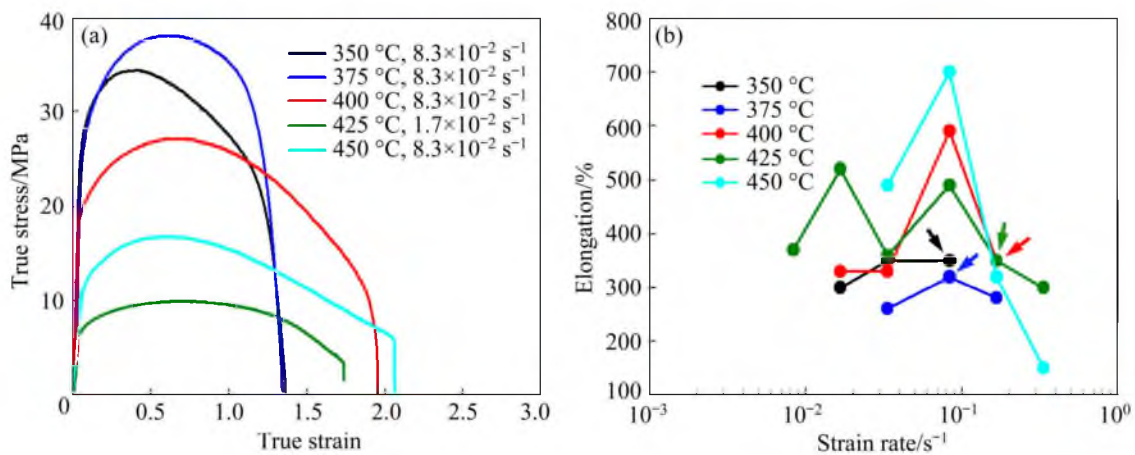

Fig. 4 True stress−true strain curves of welds exhibiting the highest elongation-to-failure at different temperatures (a) and effect of nominal strain rate on elongation-to-failure (b) (In (b), arrows indicate specimens exhibiting the most uniform elongation)

Table 1 Effect of superplastic conditions on ductility and failure location

Condition	Deformation temperature/°C	Nominal strain rate/s^{-1}	Elongation-to-failure/%	Failure location
Within superplastic range	400	8.3×10^{-2}	590	
	425	1.7×10^{-2}	520	Transition zone
	450	8.3×10^{-2}	700	
Beyond optimal superplastic range	350	3.3×10^{-2}	350	Stir zone
	375	8.3×10^{-2}	330	Base material
	400	1.7×10^{-1}	300	Transition zone
	425	1.7×10^{-1}	350	Stir zone
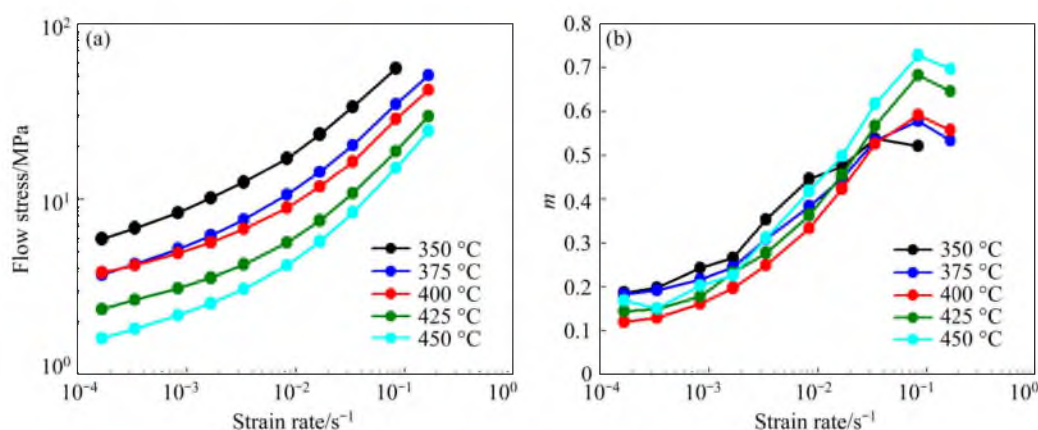
Fig. 5 Variations of flow stress (a) and strain rate sensitivity parameter (*m*) (b) as function of nominal strain rate at different temperatures

The influence of the nominal strain rate on elongation-to-failure is shown in Fig. 4(b). Below 400 °C, the welded material exhibited a comparatively weak dependence on the strain rate and showed relatively low ductility of 250%−350%. At higher temperatures, in contrast, the welded specimens demonstrated the typical superplastic behavior being very sensitive to the strain rate. Specifically, the highest ductility was observed at the nominal strain rate of ~10^{-1} s^{-1}. As expected, the elongation-to-failure tended to increase with the increase of deformation temperature, thus reaching ~700% at 450 °C.

The combined effect of strain rate and temperature on flow stress (derived from the strain-rate-jump tests) is summarized in Fig. 5(a). In accordance with expectations, the flow stress decreased with increasing deformation temperature but increased with increasing strain rate. Below 400 °C, the relationship between the flow stress and the strain rate was nearly linear. At higher temperatures, however, it approached the sigmoidal-type dependence, thus demonstrating the typical superplastic behavior (At the strain rates $\geq 2 \times 10^{-1}$ s^{-1}, no steady-state flow was found, and thus, these data were not included in Fig. 5(a)) [17,18].

To provide additional insight into the mechanical performance of the welded material, the strain rate sensitivity parameter (*m*) [17,18] was evaluated (Fig. 5(b)). At the strain rates below 1×10^{-2} s^{-1} (Here and hereafter, the upper magnitude of the strain-rate-jump test was used to relate strain rate with *m* value [14]), the magnitude of this parameter did not exceed 0.4, thus indicating marginal superplastic properties. At higher strain rates, the *m* value was typically above 0.5, thereby reflecting the typical superplastic material flow. The highest *m* value (≥ 0.5) was measured at the strain rate of ~10^{-1} s^{-1}. This mirrored the ductility behavior (Figs. 4(b) and 5(b)), thus confirming the close correlation between these characteristics [19].

3.3 Strain distribution within welded specimens

As shown in Section 3.2, the welded material exhibited the distinct superplastic behavior. Nevertheless, it is important to emphasize that the highest attained elongation of ~700% was

essentially lower than that usually measured during superplastic deformation of monolithic UFG Al−Mg−Sc alloy (i.e., >1000%) [11,13,17,19,20]. This effect was associated with fairly inhomogeneous strain distribution in the welded specimens, at least in optimal superplastic conditions (Fig. 6(a)). Specifically, the superplastic deformation was preferentially concentrated in the transition and stir zones (Fig. 6(a)) with the final failure always occurring in the transition zone (Table 1). In contrast, the base-material zone provided almost no contribution to the superplastic elongation (arrows in Fig. 6(a)). Remarkably, the failed specimens exhibited a typical pseudo-brittle fracture (high magnification insert in Fig. 6(a)), which is usually observed in optimal superplastic conditions and originates from the void coalescence.

On the other hand, the specimens tested in the conditions beyond the optimal superplastic range (i.e., at relatively low temperatures and/or high strain rates) exhibited a nearly-uniform strain distribution (Fig. 6(b)). In this case, the welded specimens failed in random locations, as shown in Table 1. In this case, the fracture surface indicated the unstable plastic flow (high magnification insert in Fig. 6(b)) intrinsic for the non-optimal superplastic conditions.

Attempting to shed light on this unusual behavior, structural response of the welded material to superplastic deformation is considered in the following section.

3.4 Microstructural evolution during super-plastic deformation

The typical pictures of microstructural evolution observed either within or beyond the optimal superplastic conditions are shown in Figs. 7 and 8, respectively. It is important to notice that the material in the grip sections only underwent static annealing at the test temperature. Depending on particular strain rate, the duration of this process ranged from 10.3 to 14.8 min. In the gauge section, the material experienced both the thermal exposure (during the holding stage of the superplastic tests) and the subsequent hot deformation. The degree of the imposed strain varied in a very wide range, depending on superplastic conditions and/or a particular microstructural zone. Nevertheless, the microstructural changes in all studied superplastic conditions were surprisingly found to be broadly similar to each other.

Specifically, the static annealing of the base material provided substantial microstructural coarsening (comparing Fig. 3(a) with Figs. 7(a) or 8(a)). On the other hand, the coarse-grained remnants were survived, and thus the micro-structure was still partially recrystallized in appearance (Figs. 7(a) and 8(a)). The relatively high stability of such remnants is thought to be due to the low dislocation density (and thus the low driving force for recrystallization) in their interior. The high thermal stability of UFG Al−Mg−Sc−Zr has also been reported in Refs. [17,21−23]. Importantly, no evidence of abnormal grain growth was found in the present work (Figs. 7(a) and 8(a)).

In the gauge section, the coarse-grained remnants completely disappeared from the base material (Figs. 7(b) and 8(b)), thus indicating that the material experienced recrystallization. This observation presumably indicated that the plastic
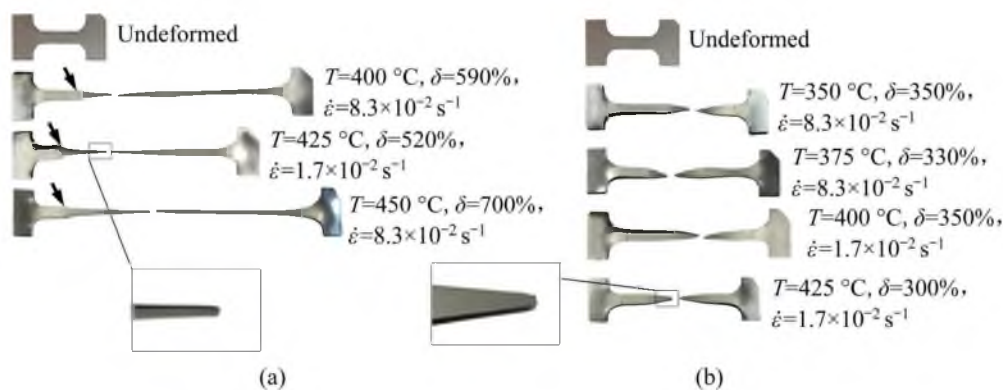

(a)   (b)

Fig. 6 Appearance of specimens tested in typical superplastic conditions (i.e., relatively high temperatures and/or low strain rates) (a), and beyond optimal superplastic range (i.e., at relatively low temperature and/or high strain rates) (b) (In (a), arrows indicate the base material region experiencing almost no superplastic strain)
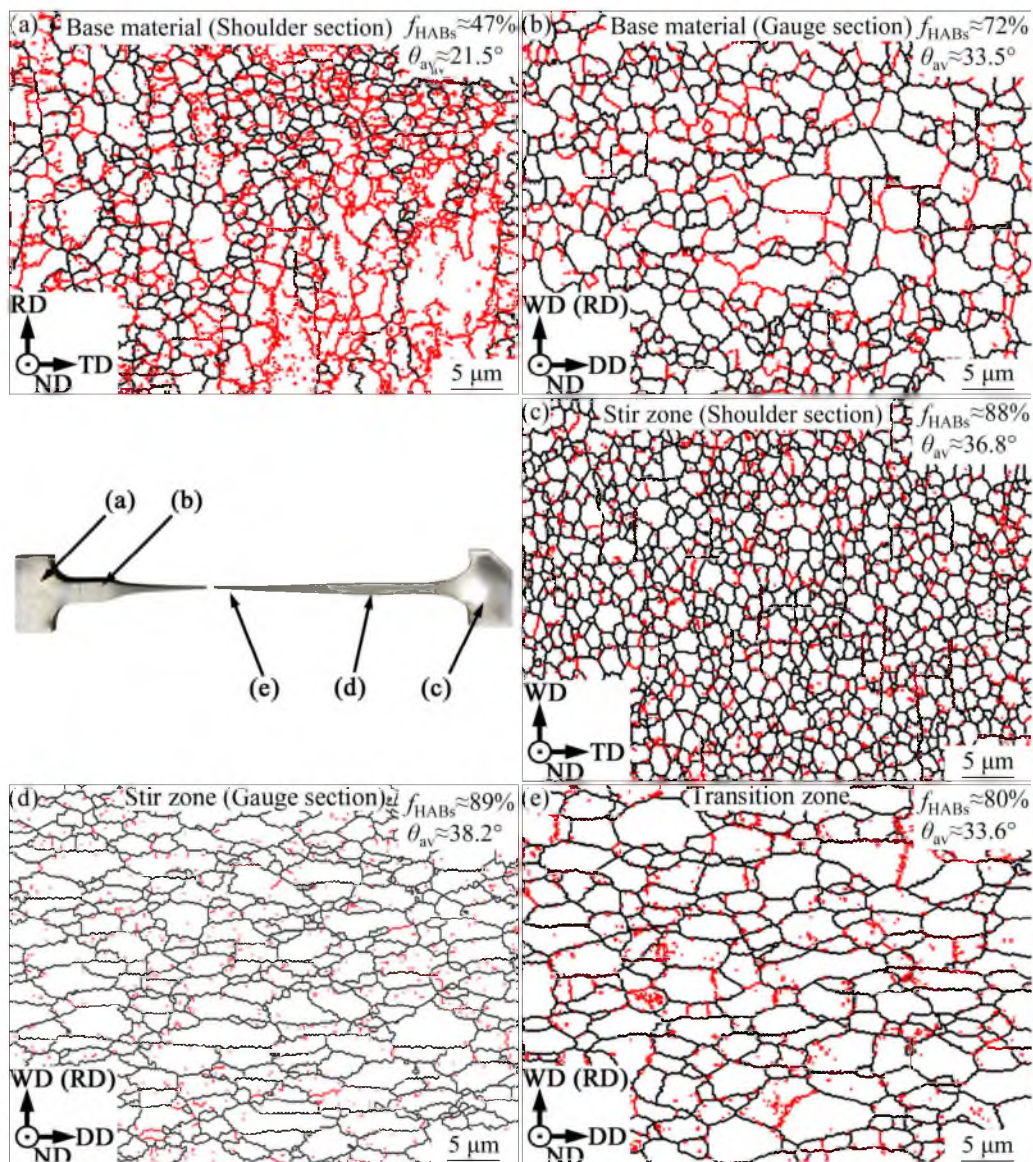
Fig. 7 EBSD grain-boundary maps showing microstructures evolved in different microstructural zones of welded sample after tensile test in optimal superplastic conditions: (a) Base material in shoulder section; (b) Base material in gauge section; (c) Stir zone in shoulder section; (d) Stir zone in gauge section; (e) Transition zone (In the maps, the LABs and HABs are depicted as red and black lines, respectively. In the inserts at the top right corner of the maps, f_{HABs} and θ_{av} indicate HABs fraction and the average misorientation, respectively. RD, WD, DD, ND, and TD denote the rolling direction, welding direction, test deformation direction, normal direction, and transverse direction, respectively. The EBSD maps were taken from the specimen tested at 425 °C and the nominal strain rate of 1.7×10^{-2} s^{-1})

deformation in the base material zone was essentially contributed by the conventional slip which promoted the recrystallization process.

The static annealing of the stir zone material also resulted in essential grain growth (comparing Fig. 3(c) with Figs. 7(c) or 8(c)). In the gauge section, the microstructural coarsening was further enhanced; moreover, the grains tended to elongate in the tensile direction (Figs. 7(d) and 8(d)). It is important to emphasize, however, that the degree of

the grain elongation was relatively small, being inconsistent with the global elongation of the tested specimen. This effect is sometimes associated with grain-boundary sliding (GBS) [18,24,25]. It is also worth noting that the strained material contained only a minor LABs fraction (Figs. 7(d) and 8(d)). Taken together, these observations suggested that material flow in the stir zone was unlikely dominated by the slip mechanism.

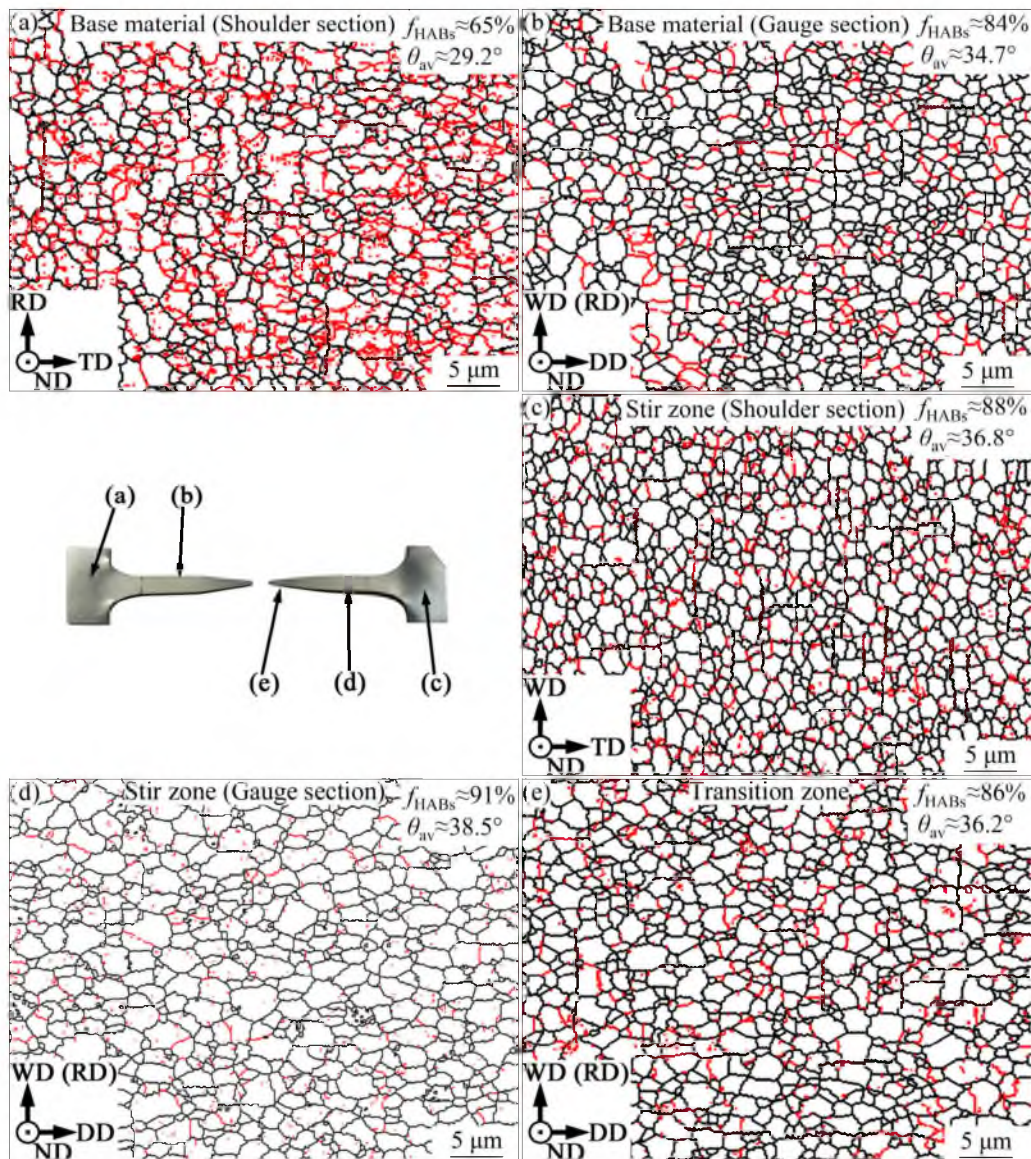As the transition zone was entirely located in

Fig. 8 EBSD grain-boundary maps showing microstructures evolved in different microstructural zones of welded sample after tensile test in conditions beyond optimal superplastic range: (a) Base material in shoulder section; (b) Base material in gauge section; (c) Stir zone in shoulder section; (d) Stir zone in gauge section; (e) Transition zone (In the maps, the LABs and HABs are depicted as red and black lines, respectively. In the inserts at the top right corner of the maps, f_{HABs} and θ_{av} indicate HABs fraction and the average misorientation, respectively. RD, WD, DD, ND, and TD denote the rolling direction, welding direction, test deformation direction, normal direction, and transverse direction, respectively. The EBSD maps were taken from the specimen tested at 425 °C and the nominal strain rate of $1.7 \times 10^{-1}\ \mathrm{s}^{-1}$)

the gauge section, its static annealing behavior was unknown. Hence, Fig. 7(e) reflected a cumulative effect of the thermal exposure and the hot strain on the microstructure. From the comparison of Fig. 7(e) or 8(e) with Fig. 3(b), it was clear that the material in the transition zone also experienced a considerable grain growth; specifically, the mean grain size was either doubled or even tripled depending on the particular test condition.

The particular interest was the formation of LABs in the grain interior, which were oriented nearly perpendicular to the tensile axis (this effect was the most pronounced in Fig. 7(e)). This may indicate that the nearly-equiaxed grain morphology observed in the gauge section was only an apparent effect associated with the rapid transformation of such transverse LABs into HABs.

4 Discussion

4.1 Activation of grain-boundary sliding mechanism

GBS is usually considered as the key straining mechanism which provides the highest superplastic ductility in UFG materials [18,23,25−30]. In order to get insight into the unusual superplastic behavior of the welded material observed in the present study, a possibility of its activation was evaluated for different deformation conditions. To this end, the theoretical flow stress associated with the GBS mechanism was calculated and compared with the experimentally measured one.

According to PEREIRA et al [27], the theoretical flow stress (σ) could be quantified as

$$\sigma = \sqrt[n]{\frac{\dot{\varepsilon}kT}{ADGb}}\left(\frac{d}{b}\right)^{p/n} G \tag{1}$$

where n is the stress exponent ($n=1/m$), $\dot{\varepsilon}$ is the nominal strain rate, k is the Boltzmann constant ($=1.38\times10^{-23}$ J/K), T is the thermodynamic temperature, A is a dimensionless constant (often taken to be 10 for UFG materials [27,28]), D is diffusion coefficient, G is shear modulus, d is the mean grain size, b is the Burgers vector amplitude ($=0.286$ nm), and p ($=2.0$) is the inverse grain size exponent.

In turn, the grain-boundary diffusion coefficient D could be determined as [26−28]

$$D = D_{0(gb)}\exp\left(-\frac{Q_{gb}}{kT}\right) \tag{2}$$

where $D_{0(gb)}$ is the vibration frequency factor and Q_{gb} is the activation energy for grain-boundary diffusion. In accordance with previous works [21,23,26−28,31], the two quantities were taken to be 1.86×10^{-4} m^2/s and 86 kJ/mol, respectively.

The temperature dependence of the shear modulus was evaluated as [21,26]

$$G = 3.022\times10^4 - 16T \tag{3}$$

Considering inhomogeneous microstructure distribution within the welded specimens (Figs. 3, 7, and 8), the local material ability to activation of the GBS mechanism was also expected to vary. In this work, appropriate predictions were made for the stir zone and the base-material zone. The relevant local strain rate data and grain size data used for such calculations are given in Table 2.

The final calculation results are summarized in Table 3. For a comparative purpose, the experimental flow stresses (measured at the true strain of ~0.1) are also shown. For the conditions beyond the optimal superplastic range, a significant difference between the predicted and measured flow stresses was typically found. Hence, the activation of the GBS mechanism was concluded to be unlikely in such cases, and the material flow was presumed to be governed by the conventional slip mechanism. Accounting for relatively low deformation temperatures and/or high strain rates in this condition range, this conclusion seems to be reasonable. Moreover, the prevalence of slip was in agreement with relatively high strain hardening observed in such deformation conditions [26] (Fig. 4(a)).

Table 2 Parameters used for calculation of grain boundary sliding stress according to Eq. (1)

Condition	Deformation temperature/°C	Nominal strain rate/s^{-1}			Mean grain size in grip section/μm	
		Entire gauge section	Stir zone section	Base material section	Stir zone	Base material
Within optimal superplastic range	400	8.3×10^{-2}	2.8×10^{-2}	2.1×10^{-1}	1.4 (1.9)*	1.5 (1.1)*
	425	1.7×10^{-2}	5.6×10^{-2}	4.2×10^{-2}	1.4 (1.9)*	1.8 (1)*
	450	8.3×10^{-2}	2.8×10^{-2}	2.1×10^{-1}	1.5 (2)*	2.3 (1)*
Beyond optimal superplastic range	350	3.3×10^{-2}	1.1×10^{-1}	8.3×10^{-2}	1.4 (1.2)*	1.4 (1.5)*
	375	8.3×10^{-2}	2.8×10^{-2}	2.1×10^{-1}	1.4 (1.2)*	1.4 (1.2)*
	400	1.7×10^{-1}	5.6×10^{-1}	4.2×10^{-1}	1.4 (1.2)*	1.8 (1.7)*
	425	1.7×10^{-1}	5.6×10^{-1}	4.2×10^{-1}	1.5 (1.2)*	1.8 (1)*

*Values in brackets show the mean grain shape aspect ratio

Table 3 Comparison of predicted stress for grain-boundary sliding with measured flow stress

Condition	Temperature/°C	Nominal strain rate/s^{-1}	Flow stress/MPa		
			Predicted		Measured*
			Stir zone	Base material	
Beyond optimal superplastic range	350	3.3×10^{-2}	97	83	32
	375	8.3×10^{-2}	62	53	32
	400	1.7×10^{-1}	61	69	30
	425	1.7×10^{-1}	26	28	22
Within optimal superplastic range	400	8.3×10^{-2}	27	29	22
	425	1.7×10^{-2}	12	13	8
	450	8.3×10^{-2}	5	7	14

*The measured flow stress for gauge section of the tensile samples including both the stir zone and base material

In contrast, a very good agreement between the calculated and experimental flow stresses was observed within the optimal superplastic range (Table 3). Accordingly, GBS was suggested as being the dominant strain mechanism. This assumption was in the line with relatively high temperatures and low strain rates in these cases.

Importantly, the predicted stresses in the base material region were higher than those in the stir zone (Table 3). In this context, it is worth noting that grain-boundary sliding is known to preferentially develop along HABs [32,33]. Considering the relatively high LAB fraction as well as the presence of the coarse-grained remnants in the base material (Figs. 3(a), 7(a), and 8(a)), the real stresses required for activation of the GBS mechanism in this microstructural region are thought to be even higher than those shown in Table 3 [23,26,28]. The specific transverse orientation of the retained coarse grains relative to tension direction (Fig. 3(a)) is thought to additionally retard the grain-boundary sliding [19,23,34,35].

4.2 Superplastic behavior of welded specimens

On the basis of the above experimental observations and theoretical considerations, the following model of superplastic behavior of the welded joints was proposed.

At low temperatures and high strain rates (i.e., beyond the optimal superplastic range), material flow was presumably governed by dislocation slip. Considering inhomogeneous microstructure distribution within the welded material (Fig. 3), the strain distribution is also expected to be non-uniform. Specifically, the yielding phenomenon is expected to occur in the relatively soft weld zone (Fig. 2). It is important to emphasize, however, that the strength difference among various microstructural regions is low (Fig. 2). Taking into account the relatively high strain hardening associated with the low-temperature slip (Fig. 4(a)), it is likely that the work hardening of the welded material rapidly achieved the base material level and thus the strain distribution became nearly uniform (Fig. 6(b)). On the other hand, dislocation slip cannot provide very large elongation, and thereby ductility of the welded specimens is relatively low (Table 1).

It is important to point out that the nearly-equiaxed morphology of grains revealed in the failed specimens (Figs. 8(b, d, e)) is not entirely consistent with the above model. As mentioned in Section 3.4, this controversy can be explained in terms of the rapid LAB-to-HAB transformation. Specifically, it is possible that the progressive development of the transverse LABs provided a pronounced subdivision of the elongated grains into the chains of nearly-equiaxed grains. However, this conception is entirely speculative at present, and therefore, the proposed model requires additional treatment.

At high temperatures and high strain rates (i.e., within the optimal superplastic range), the grain-boundary sliding presumably became to play the dominant role. As discussed in Section 4.1, this mechanism likely initiated in the stir zone and/or transition zone due to the relatively low threshold stress. It is important to emphasize that the activation of the GBS mechanism promotes

material softening (in clear contrast to dislocation slip). Hence, the local stress in the base material region cannot exceed the GBS threshold. Accordingly, once initiated, material flow tended to concentrate within the weld zone, thus giving rise to the observed strain localization (Fig. 6(a)). As activation of the GBS mechanism promotes material ductility, the welded specimens show high elongation-to-failure even despite the pronounced strain localization.

The retardation of grain-boundary sliding in the base material region is believed to be mainly due to the relatively high LABs fraction. Hence, the observed strain localization is virtually a result of a significant difference in HABs proportion between the base material and the weld zone in the as-welded material condition (Fig. 3).

5 Conclusions

(1) Despite the careful selection of FSW conditions, microstructure distribution within the welded material was not entirely uniform. Specifically, UFG in the base material zone was characterized by a relatively high LABs fraction and a significant portion of retained coarse-grained remnants.

(2) In the entire studied deformation range, the welded specimens exhibited superplastic behavior. In the optimal superplastic conditions (400−450 °C, 1.7×10^{-2}−8.3×10^{-2} s^{-1}), the recorded elongation-to-failure was of 520%−700%. Beyond the optimal superplastic range, the material ductility was 300%−350%.

(3) In the optimal superplastic conditions, strain distribution within the welded specimens was found to be fairly inhomogeneous. Specifically, material flow was almost completely concentrated in the weld zone, whereas the base material zone provided an only negligible contribution to the global elongation-to-failure. Beyond the optimal superplastic range, the strain distribution within the welded material was nearly uniform.

(4) Microstructural observations revealed significant microstructural coarsening during superplastic tests. In all microstructural zones of the welded material, the mean grain sizes were nearly doubled or even tripled, depending on particular deformation temperature or strain rate. It is important to emphasize, however, that the grain growth process progressed in a continuous manner, and no evidences of the abnormal grain growth were found.

(5) On the basis of theoretical analysis, it was found that material flow in the optimal superplastic condition was likely governed by the grain-boundary sliding mechanism. Beyond the optimal condition range (i.e., at low temperatures and high strain rates), the superplastic deformation was deduced to be essentially contributed by the conventional slip mechanism.

(6) The inhomogeneous strain distribution in the optimal superplastic conditions was attributed to the retardation of grain-boundary sliding in the base material zone due to the relatively high LABs fraction in this microstructural region.

References

[1]   POLMEAR I J. Light alloys: From traditional alloys to nanocrystals [M]. 4th ed. Oxford: Elsevier/Butterworth-Heimemann, 2006.

[2]   VALIEV R Z, LANGDON T G. Principles of equal-channel angular pressing as a processing tool for grain refinement [J]. Progress in Materials Science, 2006, 51: 881−981.

[3]   MALOPHEYEV S, KULITSKIY V, KAIBYSHEV R. Deformation structures and strengthening mechanisms in an AlMgScZr alloy [J]. Journal of Alloys and Compounds, 2017, 698: 957−966.

[4]   TANG Lei, PENG Xiao-yan, HUANG Ji-wu, MA Ai-bin, DENG Ying, XU Guo-fu. Microstructure and mechanical properties of severely deformed Al−Mg−Sc−Zr alloy and their evolution during annealing [J]. Materials Science and Engineering A, 2019, 754: 295−308.

[5]   KULITSKIY V, MALOPHEYEV S, MIRONOV S, KAIBYSHEV R. Grain refinement in an Al−Mg−Sc alloy: Equal channel angular pressing versus friction-stir processing [J]. Materials Science and Engineering A, 2016, 674: 480−490.

[6]   MALOPHEYEV S, KULITSKIY V, GAZIZOV M, KAIBYSHEV R. Mechanism of grain refinement during equal-channel angular pressing in an Al−Mg−Sc alloy [J]. Reviews on Advanced Materials Science, 2016, 47: 26−41.

[7]   SAKAI T K, BELYAKOV A, KAIBYSHEV R, MIURA H, JONAS J J. Dynamic and post-dynamic recrystallization under hot, cold and severe plastic deformation conditions [J].

Progress in Materials Science, 2014, 60: 130−207.

[8]   THREADGILL P L, LEONARD A J, SHERCLIFF H R, WITHERS P J. Friction stir welding of aluminium alloys [J]. International Materials Reviews, 2009, 54: 49−93.

[9]   MISHRA R S, MA Z Y. Friction stir welding and processing [J]. Materials Science and Engineering R, 2005, 50: 1−78.

[10] MALOPHEYEV S, MIRONOV S, KULITSKIY V, KAIBYSHEV R. Friction-stir welding of ultra-fine grained sheets of Al−Mg−Sc−Zr alloy [J]. Materials Science and Engineering A, 2015, 624: 132−139.

[11] CHEN Yu, DING Hua, MALOPHEYEV S, KAIBYSHEV R, CAI Zhi-hui, YANG Wen-jing. Influence of multi-pass friction stir processing on microstructure and mechanical properties of 7B04-O Al alloy [J]. Transactions of Nonferrous Metals Society of China, 2017, 27: 789−796.

[12] CHEN Yu, DING Hua, LI Ji-zhong, ZHAO Jing-wei, FU Ming-jie, LI Xiao-hua. Effect of welding heat input and post-welded heat treatment on hardness of stir zone for friction stir-welded 2024-T3 aluminum alloy [J]. Transactions of Nonferrous Metals Society of China, 2015, 25: 2524−2532.

[13] MALOPHEYEV S, MIRONOV S, VYSOTSKIY I, KAIBYSHEV R. Superplasticity of friction-stir welded Al−Mg−Sc sheets with ultrafine-grained microstructure [J]. Materials Science and Engineering A, 2016, 649: 85−92.

[14] VENKADESAN S, RODRIGUEZ P, PADMANABHAN K A, SIVAPRASAD P V, PHANIRAJ C. Flow transients during strain rate jump tests in a titanium-modified austenitic stainless steel [J]. Materials Science and Engineering A, 1992, 154: 69−74.

[15] HUMPHREYS F J. Quantitative metallography by electron backscattered diffraction [J]. Journal of Microscopy, 1999, 195: 170−185.

[16] HEIDARZADEH A, MIRONOV S, KAIBYSHEV R, ÇAM G, SIMAR A, GERLICH A, KHODABAKHSHI F, MOSTAFAEI A, FIELD D P, ROBSON J D, DESCHAMPS A, WITHERS P J. Friction stir welding/processing of metals and alloys: A comprehensive review on microstructural evolution [J]. Progress in Materials Science, 2021, 117: 100752.

[17] MUSIN F, KAIBYSHEV R, MOTOHASHI Y, ITOH G. Superplastic behavior and microstructure evolution in a commercial Al−Mg−Sc alloy subjected to intense plastic straining [J]. Metallurgical and Materials Transactions A, 2004, 35: 2383−2392.

[18] KAIBYSHEV O A. Superplasticity of alloys, intermetallides and ceramics [M]. Heidelberg: Springer-Verlag, 1992.

[19] LIU Feng-chao, XUE Peng, MA Zong-yi. Microstructural evolution in recrystallized and unrecrystallized Al−Mg−Sc alloys during superplastic deformation [J]. Materials Science and Engineering A, 2012, 547: 55−63.

[20] DUAN Yu-lu, XU Guo-fu, TANG Lei, LIU Yun, XU Jia-wei, DENG Ying, YIN Zhi-min. Excellent high strain rate superplasticity of Al−Mg−Sc−Zr alloy sheet produced by an improved asymmetrical rolling process [J]. Journal of Alloys and Compounds, 2017, 715: 311−321.

[21] PEREIRA P H R, HUANG Y, LANGDON T G. Examining

the microhardness evolution and thermal stability of an Al−Mg−Sc alloy processed by high-pressure torsion at a high temperature [J]. Journal of Materials Research and Technology, 2017, 6: 348−354.

[22] AVTOKRATOVA E, SITDIKOV O, MUKHA-METDINOVA O, MARKUSHEV M, MURTY S V S N, PRASAD M J N V, KASHYAP B P. Microstructural evolution in Al−Mg−Sc−Zr alloy during severe plastic deformation and annealing [J]. Journal of Alloys and Compounds, 2016, 673: 182−194.

[23] NIEH T G, HSIUNG L M, WADSWORTH J, KAIBYSHEV R. High strain rate superplasticity in a continuously recrystallized Al−6%Mg−0.3%Sc alloy [J]. Acta Materialia, 1998, 46: 2789−2800.

[24] MACKENZIE J K. Second paper on statistics associated with the random disorientation of cubes [J]. Biometrika, 1958, 45: 229−240.

[25] MASUDA H, SATO E. Diffusional and dislocation accommodation mechanisms in superplastic materials [J]. Acta Materialia, 2020, 197: 235−252.

[26] YUZBEKOVA D, MOGUCHEVA A, KAIBYSHEV R. Superplasticity of ultrafine-grained Al−Mg−Sc−Zr alloy [J]. Materials Science and Engineering A, 2016, 675: 228−242.

[27] PEREIRA P H R, HUANG Y, KAWASAKI M, LANGDON T G. An examination of the superplastic characteristics of Al−Mg−Sc alloys after processing [J]. Journal of Materials Research, 2017, 32: 4541−4553.

[28] LANGDON T G. A unified approach to grain boundary sliding in creep and superplasticity [J]. Acta Metallurgica et Materialia, 1994, 42: 2437−2443.

[29] KAWASAKI M, LANGDON T G. Principles of superplasticity in ultrafine-grained materials [J]. Journal of Materials Science, 2007, 42: 1782−1796.

[30] KAWASAKI M, BALASUBRAMANIAN N, LANGDON T G. Flow mechanisms in ultrafine-grained metals with an emphasis on superplasticity [J]. Materials Science and Engineering A, 2011, 528: 6624−6629.

[31] KAWASAKI M, LANGDON T G. Review: Achieving superplasticity in metals processed by high-pressure torsion [J]. Journal of Materials Science, 2014, 49: 6487−6496.

[32] KAWASAKI M, LANGDON T G. Review: Achieving superplastic properties in ultrafine-grained materials at high temperatures [J]. Journal of Materials Science, 2016, 51: 19−32.

[33] KAIBYSHEV R, SHIPILOVA K, MUSIN F, MOTOHASHI Y. Achieving high strain rate superplasticity in an Al−Li−Mg alloy through equal channel angular extrusion [J]. Materials Science and Technology, 2005, 21: 408−418.

[34] KAIBYSHEV O A, PSHENICHNIUK A I, ASTANIN V V. Superplasticity resulting from cooperative grain boundary sliding [J]. Acta Materialia, 1998, 46: 4911−4916.

[35] MASUDA H, KANAZAWA T, TOBE H, SATO E. Dynamic anisotropic grain growth during superplasticity in Al−Mg−Mn alloy [J]. Scripta Materialia, 2018, 149: 84−87.

搅拌摩擦焊超细晶 Al−Mg−Sc−Zr 合金的超塑性行为

I. VYSOTSKIY, K. KIM, S. MALOPHEYEV, S. MIRONOV, R. KAIBYSHEV

Belgorod National Research University, Pobeda 85, Belgorod 308015, Russia

摘　要：研究提高搅拌摩擦焊超细晶(UFG)Al−Mg−Sc−Zr 合金接头超塑性的新工艺。为了抑制严重变形基体材料中通常出现的异常晶粒长大现象，在高温下制备 UFG 材料。结果表明，新工艺路线可以降低 UFG 组织中的位错密度，从而提高其热稳定性。然而，新方法导致相对较高的小角度晶界比例，从而在随后的超塑性试验中延缓晶界滑动。因此，尽管成功抑制了基材区晶粒的异常长大，但超塑性变形仍优先集中在完全再结晶搅拌区材料中，从而导致最大断裂伸长率未超过 700%。
关键词：铝合金；等径角挤压；搅拌摩擦焊；超细晶材料；超塑性

(Edited by Wei-ping CHEN)